fractal and fractional

MDPI

*Article*

# Fractal Analysis of Polarizability in Graphite Deposits: Methodological Integration for Geological Prediction and Exploration Efficiency

**Yuqi Liang [1,2], Qinglin Xia [1,*], Kenan Jiang [2] and Ercheng Pang [2,*]**

[1] School of Earth Resources, China University of Geoscience, Wuhan 430074, China; liangrui829@126.com
[2] 217 Team of Shanxi Geological Group, Datong 037008, China
* Correspondence: qlxia@cug.edu.cn (Q.X.); 13753278414@163.com (E.P.); Tel.: +86-136-5720-8280 (Q.X.)

**Abstract:** Most geophysical and geochemical data are commonly acknowledged to exhibit fractal and multifractal properties, but the fractal characteristics of polarizability have received limited attention from the literature. The present study demonstrates that the polarizability data of the graphite deposits have fractal characteristics and introduces the fractal method for its quantitative analysis to indicate and predict the properties of graphite deposits. The results show that the concentration-area (C-A) method is superior to classical interpolation in anomaly extraction but inferior to the spectrum-area (S-A) method in the coverage region. Because the type of graphite ore is sedimentary-metamorphic in this area, the graphite ore-bodies can be regarded as a special stratum, which is different from most metal deposits, and the anomaly of graphite ore are shown in the background mode of the S-A method. The high values of the background mode effectively indicate the potential areas where the graphite-bearing strata occur, while observing a decrease in the power-law exponent ($\beta$) of the background mode as the width of ore-bodies increases. The validity of this conclusion was confirmed based on the vertical profiles of the predicted area, and the uncharted ore vein was thereby identified. Furthermore, it was found that the anomaly mode can serve as a grade indicator of graphite ore rather than delineating the fault. By integrating the background and anomaly modes of the S-A method, we can quantitatively predict and effectively identify high-grade targets from sedimentary deposits containing minerals in future exploration.

**Keywords:** anomaly mode; background mode; fractal; graphite; polarizability; power-law exponent

check for updates

**Citation:** Liang, Y.; Xia, Q.; Jiang, K.; Pang, E. Fractal Analysis of Polarizability in Graphite Deposits: Methodological Integration for Geological Prediction and Exploration Efficiency. *Fractal Fract.* **2024**, *8*, 198. https://doi.org/10.3390/fractalfract8040198

Academic Editor: Zine El Abiddine Fellah

Received: 20 February 2024
Revised: 21 March 2024
Accepted: 25 March 2024
Published: 29 March 2024



## 1. Introduction

Fractals are objects featuring scale invariance [1,2]. Geological processes have multistage and spatial correlation; thus, geological events and anomaly information have spatial self-similarity or statistical self-similarity, which match a fractal or multifractal distribution [3,4]. Based on the fractal theory, the concentration-area (C-A) [5] and the spectrum-area (S-A) [6] methods were established in the spatial domain and frequency domain, respectively, using density-scale fractal model [7]. These two methods follow the power-law distribution and have been widely used in the analysis of geophysical and geochemical data [8–11]. However, fractal method is rarely applied into the polarizability data of the induced polarization. Due to variations in electrical conductivity among different rock types, similar to the variances in elemental abundance within soil, this indicates that the anomalous information of polarizability data can be extracted and classified using fractal methods. Daneshvar et al. [12] used the concentration-volume (C-V) fractal method to process the polarizability data of the Cu-Mo deposit and obtained relatively accurate results in Ireland, which showed that the polarizability data can be processed by fractal methods to distinguish conductive veins from the surrounding rocks. Due to the fact that graphite has good electrical conductivity, the graphitic ore has the characteristics of low resistance and high polarization compared with surrounding rock. Therefore, the induced polarization method is a good indicator for graphite ore prospecting, especially the polarizability [13]. Furthermore, the energy spectral density of graphite ore can show global and local self-similarity in its polarization anomaly [14], and the occurrence mode of graphite ore can be well reflected in the low-frequency signal of the frequency domain [15]. Therefore, we verified that the polarizability data have fractal characteristics and utilized the S-A method in this study to indicate and predict the abnormal information of graphite deposits.

The power spectrum of S-A can be applied to indicate the spatial variability and the smoothing degree of geological features, including the ore-bodies [16–18]. The S-A method can be decomposed into the anomaly mode and the background mode, according to different power-law exponents in the frequency domain; among these, the background mode can reflect the characteristics of geological units [19]. The genetic type of graphite deposits is sedimentary-metamorphic in Xinrong District [20], and the graphite ore can be considered a unique stratum. Therefore, we used the background mode to indicate the graphite-bearing gneiss. Most studies only used the self-similarity of the data to extract and grade anomalies [4–9,11,13–16], without studying whether the fractal dimension in the fitting curve has particular geological significance. Fractal dimensions not only describe the complexity of the fault distribution and the maturity of tectonic evolution but also reflect the degree of mineralization.

For this, we knew that the power-law exponent ($\beta$) refers to the log-log slope of the power spectrum, and the relationship between $\beta$ and the fractal dimension ($D$) is given by: $\beta = 5 - 2D$ [21]. Xia et al. observed that the relationship between $\beta$ and $D$ can be represented by: $\beta = 4 - 2D$ [22]. Cheng named the power-law exponent of the fractal curves as the singularity index ($\alpha$) [23]. The power-spectral dimension is shown to be invariant to arbitrary scaling by direct computation [24,25], and the lacunarity and anisotropy do not significantly affect the estimation of dimensions from the power spectrum [26]. Considering the relationship between $\beta$ and $D$, the value of $\beta$ is invariant in the power spectrum. In the current study, we investigated the geological significance of $\beta$ in the S-A model: $A(>s) \propto S^{-\beta}$ [27], which focuses on the stochastic notion of spatial correlation and the variability by spectrum [28,29]. In this way, we determined the relationship between the width of the ore-bodies and the power-law exponent ($\beta$) of the background mode. The anomaly mode has a high-pass filtered pattern to indicate the spatial variability for predicting the mineralization. Recent related research on metal ore has used the anomaly mode to identify the local structure [30,31], thus non-metallic ores are less studied in this respect. Therefore, the objective of this study was to ascertain the significance of the high polarization values of the anomaly mode with respect to the graphite ore.

## 2. Geological

The Xinrong graphite ore belt is located at the contact zone between the khondalite belt and the central orogenic belt in the north of the North China Craton (NCC). At present, there are seven exploration areas within the ore belt spanning approximately 22 km, and 52 million tons of crystalline graphite have been identified. The characteristics and resources of the ore-bodies are shown in Table 1 [20]. In this area, the Huangtuyao Formation of the Jining Group in the Middle Archaean are the main outcrop layer, which contains two rock types: graphite-bearing gneiss and garnet-bearing gneiss. The distribution of graphite-bearing gneiss is mostly stratified and a little lenticular, and lots of diabase belts with NW in the Luliang stage developed, which play a role in fracturing the ore-bodies [32,33]. In addition, the scattered Zumabao Formation of Cretaceous and the Yungang Formation of Mid-Jurassic are only exposed in the south of Figure 1.

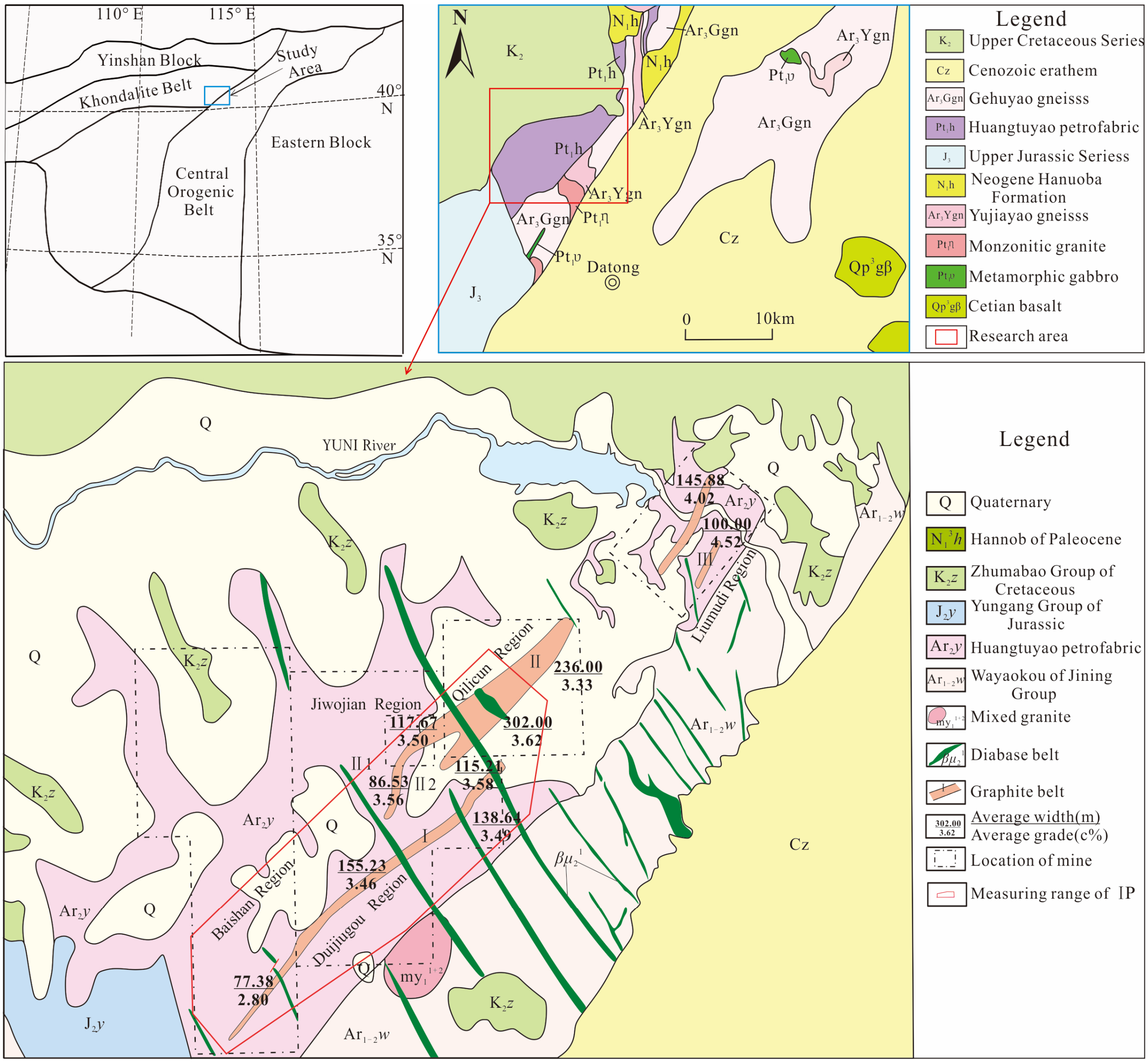


**Figure 1.** Regional geological map of the Xinrong graphite ore belt in Datong, Shanxi.

**Table 1.** Characteristics of ore-bodies in Xingrong area.

| Name of Mine | Ore-Belt Number | Average Width (m) | Average Grade (c%) | Graphite Resources (Million Tons) | Research Partition | Reference |
|---|---|---|---|---|---|---|
| Baishan | I | 77.38 | 2.80 | 3.4123 | D | [34] |
| Duijiu gou | I | 155.23 | 3.46 | 5.7547 | E | [33] |
| | | 138.64 | 3.49 | | F | |
| | $II_1$ | 86.53 | 3.56 | | B | |
| Jiwojian | $II_1$ | 117.67 | 3.50 | 0.7689 | | |
| Qilicun | $II_2$ | 115.21 | 3.58 | 28.2246 | | |
| | II | 302.00 | 3.62 | | C | |
| | | 236.00 | 3.33 | | | |
| Liumudi | $III_1$ | 145.88 | 4.02 | 2.2700 | | [35] |
| | $III_2$ | 100.00 | 4.52 | | | |

## 3. Methods

### *3.1. Fractal Method*

Usually, the geological phenomena of fractals generated in the statistical sense are self-similar [1]. The C-A and S-A methods are widely used mathematical geological methods, which are used in this study.

The fractal model:

$$N(r) = Cr^{-D},$$

where $C$ is the proportional coefficient, $D > 0$, is the fractal dimension, $r$ means concentration or spectrum of the polarizability, and $N(r)$ is a statistic of quantities greater than $r$. Using this method, the values of contours and their enclosed areas on the geophysical and geochemical maps can be plotted on log-log paper. The values corresponding to a set of similarly shaped contours will show a power-law relationship between the contour values and the enclosed areas. Distinct patterns represented by the contours can be separated by different straight-line segments with different slopes fitted to the values of contours and the enclosed areas on the map. In the log-log plot, the $D$ value is the slope of the fitting line, and $R^2$ is the fitting degree of the line. The background value and abnormal values can be distinguished by different slope values, while the value of r at the intersection of the lines is defined as the threshold [8].

The analysis of the spatial-frequency distributions plays a crucial role in quantitative assessments of mineral resources [19]. The power spectrum reveals information about the relative amount and amplitude of different wavelength features in the form of a profile or different frequency components in the form of a time series [25]. Signals or patterns in a spatial domain can be decomposed into different components, each of them has a specific frequency range, and Fourier transformation can be used to convert signals from a spatial domain into the frequency domain. The S-A method has been used to convert the characteristics and patterns from the original image into the frequency domain by the Fourier transform, and also been used to measure the frequency of complex spatio-temporal anomalies [6]. The S-A model follows a power-law relationship:

$$\mathrm{A}(>\mathrm{s}) \propto S^{-\beta}$$

Which can be decomposed into the anomaly mode and background mode with different power-law exponents. The two modes can then be applied separately to indicate the spatial variability and the smoothing degree of geological features. The S-A method can reflect the geological features and spatial variability of ore-bearing gneiss in sedimentary-metamorphic graphite deposits as a stratum.

### *3.2. Induced Polarization (IP)*

The induced polarization (IP) method is effective applied to conductive minerals and oil reservoirs [36–38] by extracting the resistivity and polarization information of different rocks [39]. The principle of the IP method lies in the occurrence of distinct potential lag values in current and voltage during the process of charging and discharging to the ground, attributed to variations in conductive mineral distribution within the rock [40,41]. Polarizability is used to describe the degree of dissipation of its voltage over time, that is, to measure the difficulty of electrode reaction during charge and discharge [42]. Because there is a large conductivity contrast between graphite minerals and the surrounding rocks [43], even the graphite concentration is low, there will be an IP response, which makes the IP method has particular significance for the exploration and development of graphite ore [44,45].

Time domain-induced polarization (TDIP) and frequency domain-induced polarization (FDIP) are two different types of IP methods [46], and TDIP was used to analyze the abnormal properties of graphite ore in this research.

## 4. Data Preparation

The physical properties of rocks are the geophysical premise and basis of anomaly interpretation [47]. In order to clarify the physical properties of rocks in this area, 115 rocks of 4 types were sampled, and their polarizability (η) and resistivity (ρs) were measured. The results are shown in Table 2. The data show that the polarization values of all the rocks except graphite gneiss are low. The maximum is less than 7, and the average is about 2. The polarization value of graphite gneiss is obviously greater than that of other rocks, indicating that the graphite anomaly can be well represented by their polarizability.

The set of TDIP measurement is as follows: The orientation of the line is 315°, orthogonal to the ore body. On a 100 × 20 m grid, the polarizability and resistivity data of 10,000 points were collected with the accuracy of 0.01. The current supplied was more than 1 A, and the measurement period was 32 s. To improve the working efficiency and increase the exploration depth, the distance between the two power supply stages (AB) was set at 1600 m and the measuring distance (MN) was 40 m based on empirical knowledge in this area, which is twice the distance between the measuring points [34]. Vertical polarizability data are measured with AB (4~800 m) and MN (2~40 m), and each profile has at least four measuring points. The errors of the measurement results are in accordance with the relevant regulations [33].

**Table 2.** Physical parameters of Xingrong area.

| Type of Rock | Number of Specimens | Polarizability (η) (%) | | Resistivity (ρs) (Ω·m) | |
|---|---|---|---|---|---|
| | | Range | Mean | Range | Mean |
| Mixed granite | 35 | 0.93–4.24 | 2.05 | 12.4–884.2 | 54.0 |
| Garnet gneiss | 28 | 0.68–5.11 | 2.24 | 5.3–1085.0 | 186.0 |
| Graphite gneiss | 40 | 1.10–41.50 | 13.34 | 3.5–918.0 | 36.1 |
| Diabase | 12 | 0.49–6.92 | 3.62 | 15.5–671.2 | 282.2 |

The distribution range of low-resistivity areas in this region is relatively large, including areas with high polarization rates [34]. According to the characteristics of "low resistance and high polarization", it is considered that the distribution range and occurrence of graphite ore can be directly inferred from the polarizability data in this area. For the statistical analysis, the maximum value of the horizontal polarizability data in this area was 31.88, the minimum value was 1.02, the average (AVG) was 8.87, and the standard deviation (σ) was 4.81. The minimum outlier obtained using the standard normal distribution was 13.68 (AVG + σ), and the anomaly was divided into three types using the multiples of the standard deviations as the threshold, with the values being 18.49 (AVG + 2σ) and 23.30 (AVG + 3σ).

The polarizability value (η) was used as $r$ for statistical the $N(r)$, with a precision of 0.01. The values of $r$ and $N(r)$ were carried out by using the log-log figure based on the C-A method. Figure 2a shows that the logarithmic curve of the entire polarizability data is smooth and in conformance with the power-law distribution: $y = 3.962 - 0.385x^{5.249}$, which illustrates that the polarizability data have fractal characteristics [2]. The pattern shows two general linear trends, which have been used to distinguish the anomaly and background [5]. Using the least-square (LS) method to fit the straight line, the slopes and fitting degree of the line were −0.2127 and −6.3442 (slopes) and 0.8513 and 0.954 (fitting degrees), respectively. The two lines intersected at $\lg(r) = 1.069$ ($r = 11.72$), indicating that the polarizability value ($r \geq 11.72$) are the anomaly. Compared to the minimum anomaly value obtained by the standard normal distribution, the anomaly value of the C-A method was obviously lower. Additionally, we analyzed the anomaly of the C-A method by multifractal and categorized it into three linear segments in Figure 2b. The slopes and fitting degrees of them were −3.3851, −7.2259 and −9.7757 (slopes), and 0.9924, 0.9960 and

0.9960 (fitting degree), respectively. The results show that the classification thresholds of abnormal information are 17.70 and 21.00.

For verifying the reliability of the anomaly, we generated the log-log map of $r$ and $N(r)$, corresponding to the threshold values of the normal distribution. Three straight lines were fitted to the different anomalies in Figure 2c. The slopes and fitting degrees of the three lines are −3.9494, −8.1578, and −9.4408 (slopes) and 0.9908, 0.9950, and 0.9878 (fitting degree), respectively. This indicated that the classification thresholds of abnormal information using the normal distribution are 18.48 and 23.30. The results suggested that the fitting degree of the C-A method for classifying the anomaly was higher than that of the standard method in each category, indicating the anomaly had a higher correlation, which was extracted and graded by the C-A method. Although the range of intermediate anomalies was narrow in the C-A model, the minimum and maximal value of anomalies using the C-A method were lower than those with the standard method. This suggested that the anomalies had a wider range of anomaly detection boundaries and a higher accuracy for the best anomaly intensity, which were extracted by the C-A method. Therefore, the C-A method was better than the standard method for determining the anomaly threshold of classification.

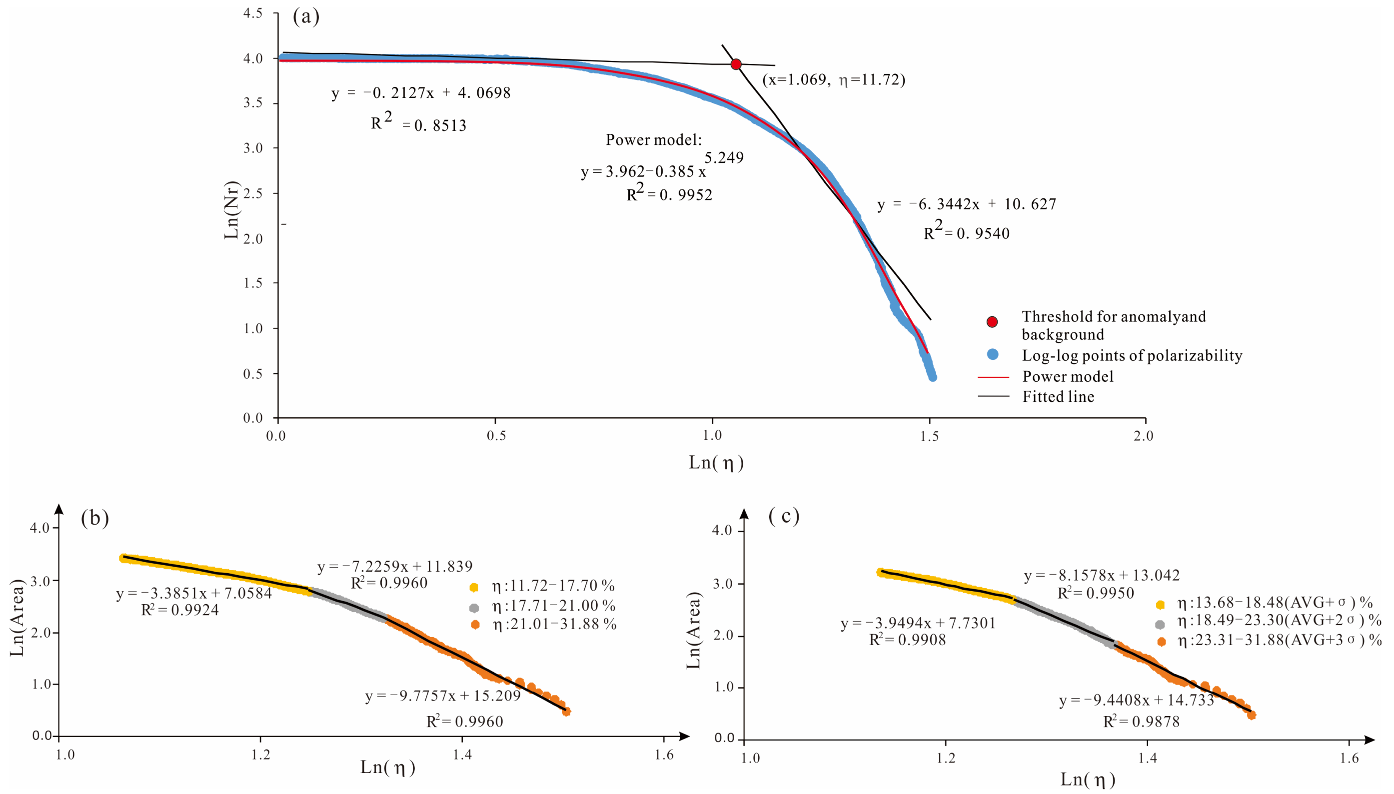


**Figure 2.** Different anomaly classification methods and comparison: (**a**) The lg-lg plot of polarizability; (**b**) Anomaly classification of C-A method; (**c**) Anomaly classification of standard normal distribution.

Three different interpolation methods, natural neighbor (NN), Kriging, and inverse distance weighting (IDW), were used for comparative analysis with the same original data and the anomaly classification threshold of the standard deviations. Based on the qualitative judgment in Figure 3, the anomalies observed in all three maps exhibit a high degree of spatial continuity and align consistently with the trend of the ore-bodies in the situation. However, the contour map of Kriging could reflect the areas of high-value anomalies better than others. According to the statistical data of the abnormal region and known ore-bodies superimposition in Table 3, it can be seen that the area under curve (AUC) values of the three methods were greater than 0.7, indicating that the methods can correctly express anomalies in the polarizability interpolation. AUC value of the Kriging method was the best expressed in the receiver operating characteristic (ROC) curves in Figure 3d. Although the gap of the AUC value was not obvious, combined with the qualitative judgment, Kriging was concluded as the best interpolation method for polarization interpolation.

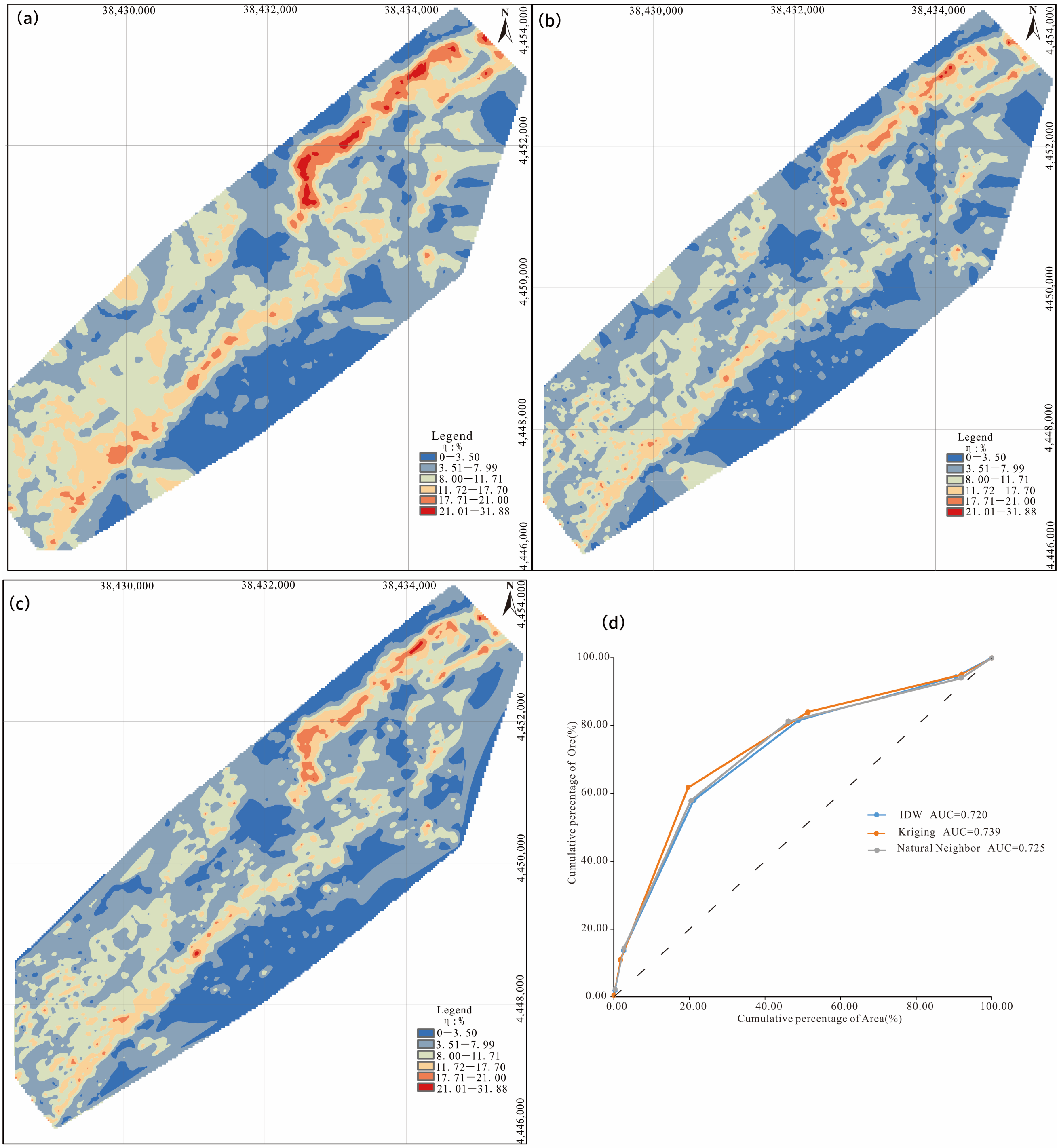


**Figure 3.** ROC curves and contour maps of polarizability data by different interpolation method: (**a**) Kriging contour map; (**b**) IDW contour map; (**c**) NN contour map; (**d**) ROC curves of three methods.

**Table 3.** The simplified calculation of the area under curve.

| Classic of Polarizability η (%) | Inverse Distance Weighting | | | Kriging | | | Natural Neighbor | | |
|---|---|---|---|---|---|---|---|---|---|
| | Area (%) | Ore (%) | AUC Value | Area (%) | Ore (%) | AUC Value | Area (%) | Ore (%) | AUC Value |
| 1 (η: 0–3.50) | 9.472 | 5.549 | 0.092 | 7.992 | 4.878 | 0.780 | 8.112 | 5.823 | 0.079 |
| 2 (η: 3.51–7.99) | 41.719 | 12.957 | 0.367 | 40.631 | 11.128 | 3.639 | 45.684 | 12.835 | 0.401 |
| 3 (η: 8.00–11.59) | 27.645 | 23.598 | 0.193 | 31.696 | 22.195 | 2.311 | 25.706 | 23.445 | 0.179 |
| 4 (η: 11.60–17.71) | 18.513 | 44.268 | 0.066 | 17.895 | 50.915 | 0.650 | 17.753 | 43.628 | 0.064 |
| 5 (η: 17.72–21.00) | 2.278 | 11.768 | 0.002 | 1.734 | 10.488 | 0.010 | 2.331 | 12.012 | 0.002 |
| 6 (η: 21.01–31.88) | 0.374 | 1.860 | 0.000 | 0.053 | 0.396 | 0.000 | 0.413 | 2.256 | 0.000 |
| Sum | 100.000 | 100.000 | 0.720 | 100.000 | 100.000 | 0.739 | 100.000 | 100.000 | 0.725 |

## 5. Results and Discussion

### *5.1. S-A Method*

We used the Kriging method to form an anomaly map with these threshold values, as shown in Figure 4a. Then, S-A method was used to derive the background as Figure 4b and anomaly modes as Figure 4c. The two modes showed different linear trends in their frequency properties. Using the least-squares method to fit the straight line, the slopes and fitting degrees of the lines were −0.077 and −0.591 (slopes) and 0.855 and 0.990 (fitting degrees) for the background and anomaly modes, respectively.

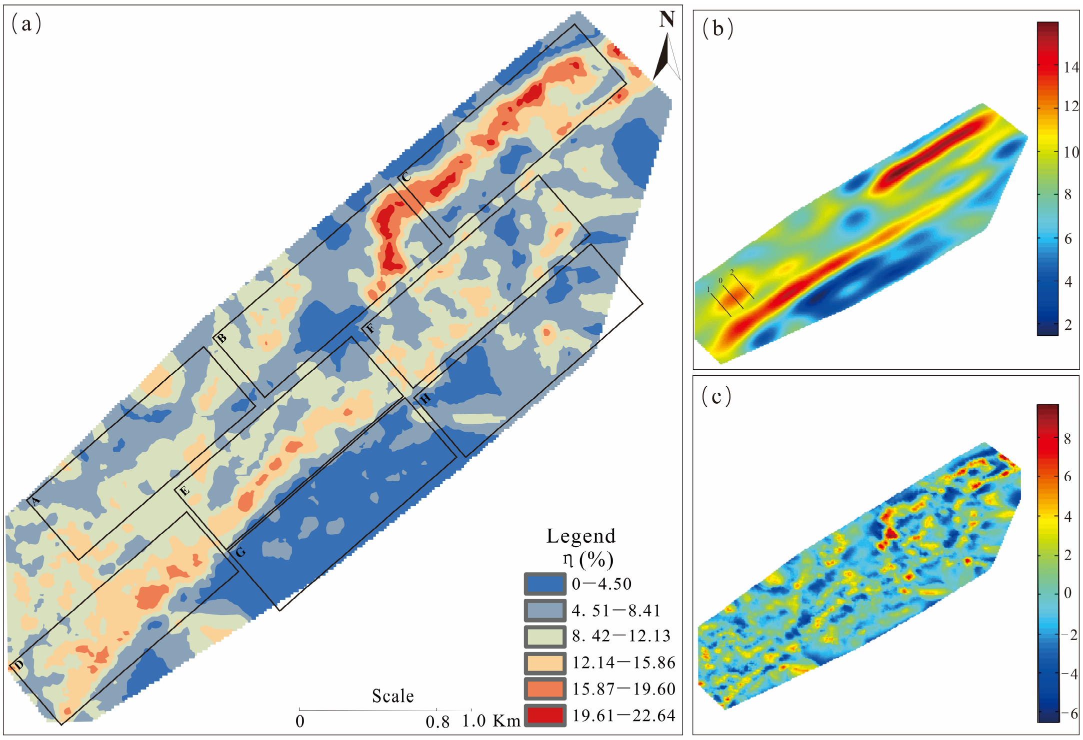


**Figure 4.** (**a**) Kriging contour map; (**b**) Background mode of the S-A method; (**c**) Anomaly mode of the S-A method.

In the S-A method, Cheng showed that the high-frequency signal (abnormal mode) decomposed by Fourier transform was caused by local mineralization anomalies, while the low-frequency signal (background mode) was affected by regional geological processes, showing an elliptical pattern controlled by rock mass and strata [7]. According to the background mode and abnormal mode decomposed by S-A method, it can be found that the anomalous features of graphite ore in this region are different from those of metal or hydrothermal deposits, and the anomaly information of the graphite ore is displayed in the background mode instead of the anomaly mode. The reason is that the origin of graphite ore deposits in this area is different from that of most metal deposits, which mainly occur in the structural parts. The graphite ore-bodies in this area are of sedimentary metamorphic origin and can be regarded as a distinct conductive stratum. Therefore, the distribution characteristics of the graphite ore-bodies will be displayed in the background field of the frequency domain.

The Kriging interpolation map could reflect the abnormal potential of graphite ore; there were some discontinuous and disordered local anomalies on the map. The high-value region in the background field, as depicted in Figure 4b, exhibits a higher degree of smoothness and continuity compared to the Kriging method in Figure 3a. Moreover, it effectively eliminates the scattered abnormal high-value points, and the high-value region is well overlaid with the known ore-bodies No. I and No. II, basically consistent with the known ore-bodies. There is a good elliptic anomaly in the northeast of No. I ore-bodies, indicating that there may be an undiscovered graphite ore vein. This abnormal range is not obvious by the C-A method, and the field investigation shows that it is caused by the thicker loess cover. Therefore, compared with the C-A method, which can only quantitatively select threshold values, the S-A method can also extract weak anomaly information from the coverage area.

To further study and estimate the graphite potential, we divided the mining area into eight zones (denoted as A through H) with dimensions of $2.5 \times 0.8$ km according to the trend of the ore-bodies in Figure 4a and analyzed the anomaly map of each zone with the S-A method. The left patterns were the anomalies, and the right patterns were the background in Figure 5. The power-law exponent ($\beta$) of the anomaly mode in those zones are $\beta$A = 0.157, $\beta$B = 0.172, $\beta$C = 0.176, $\beta$D = 0.187, $\beta$E = 0.196, $\beta$F = 0.157, $\beta$G = 0.196, and $\beta$H = 0.097, respectively. While the power-law exponent ($\beta$) of the background mode in those zones are $\beta$A = 0.628, $\beta$B = 0.581, $\beta$C = 0.570, $\beta$D = 0.630, $\beta$E = 0.614, $\beta$F = 0.610, $\beta$G = 0.643, and $\beta$H = 0.603, respectively. The fitting degree ranged from 0.938 to 0.9997, indicating that all the modes have a good fitting effect.

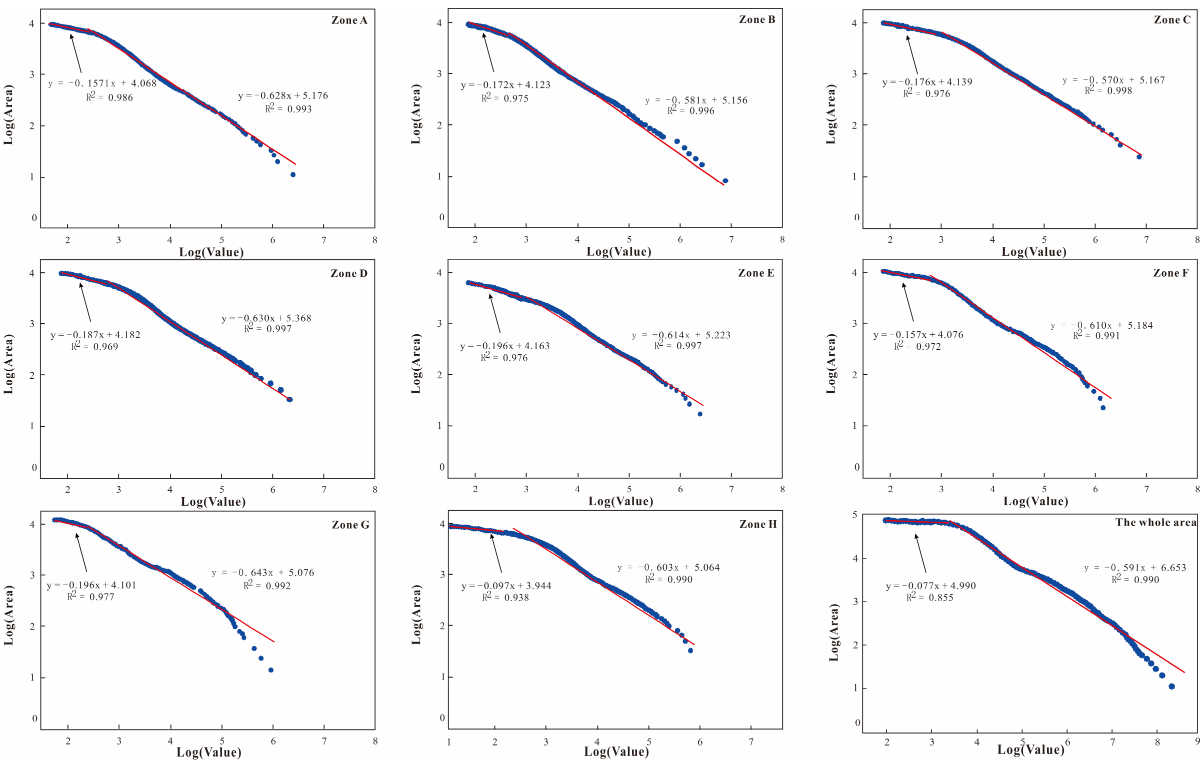


**Figure 5.** S-A gradation map of different zones.

### *5.2. Background Mode*

Due to the presence of graphite-bearing gneiss as a complete formation [20], we focused on measuring the smoothing degree of the graphite ore-bodies, which show analogous characteristics of the geological units from the background mode. The range of high values on the background mode were basically consistent with that of the two known main ore-bodies in the area, indicating that the background mode can well reflect the graphite-bearing strata. There are anomalies in the background mode to the north of the No. I ore-bodies in the Baishan region, suggesting that there may be an undiscovered ore vein in that region. For estimating the graphite potential, we investigated the characteristics of ore-bodies in different zones (shown in Table 1 and Figure 4a) and found that the high values of the background mode did not correspond with the width of the ore-bodies. However, we analyzed the width of the ore-bodies using the power-law exponent ($\beta$) of the background mode. The No. I graphite ore-bodies are distributed in the D, E, and F zones; the $\beta$ value and width of the ore-bodies in the three zones were 0.630, 0.614, and 0.610 ($\beta$), and 77.38, 155.23, and 138.64 (width), respectively. This indicates that under the same length, the $\beta$ value decrease with the widening of the ore-bodies. The No. II graphite ore-bodies are distributed in the B and C zones, and the ore-bodies narrow as they branch off in the B zone according to the geological map. The $\beta$ value in the B and C zones was 0.581 and 0.570, respectively, indicating a reduction in value as the ore-bodies under the same width increased in length. The G zone does not contain known ore-bodies and showed no reaction on the anomaly map or the background mode, and the $\beta$ value of the G zone was the highest. Therefore, we conclude that the $\beta$ value alone, rather than the entire high-value area of the background mode, can effectively represent the width of the ore-bodies. This is supported by our findings, which demonstrate a decrease in $\beta$value as the ore-bodies exhibit greater length and width. Overall, the power-law exponent ($\beta$) of the background mode from the S-A model could quantitatively reflect the width of ore-bodies.

The anomalies of the A zone were unobvious and distinctly different from those of the D zone with similar $\beta$ values on the Kriging map, and there were anomalies on the background mode in the A zone, suggesting that there may be an undiscovered ore vein in that region. According to the above inference, we suggested that the A zone should be considered to have graphite ore-bodies corresponding to the $\beta$ value, meaning the width of graphite vein is closer to 77.38 m (D zone). Because the $\beta$ value of the background mode over the whole area was 0.591, it is implied that when the $\beta$ value of each community was smaller than 0.591, the width of ore-bodies was larger than that of the average of ore-bodies. Only the $\beta$ values of the B and C zones were smaller than 0.591, and this conclusion was consistent with the actual situation. By comparing the $\beta$ values of local and whole areas, we can quantitatively select the better potential area. This demonstrates that the power-law exponent ($\beta$) of the background mode from the S-A model is an important supplement that not only provides potential information regarding graphite deposits that cannot be directly represented on the Kriging map, but also enables quantitative judgment of the width of ore-bodies in prospecting rather than making a qualitative analysis.

In order to further confirm the morphology of graphite ore-bodies in potential area, we measured the polarizability data of three vertical profiles in Figure 6. Each profile is 200 m apart, as shown in Figure 4b. The distance of the measuring points is 100 m, and the depth of measurement is 800 m. When the value of the polarizability data is greater than 12%, it indicates that the carbon content of rocks is greater than 2%, which is the threshold value of graphite ore [33–35]. According to the three vertical profiles in Figure 6, the graphite ore vein is continuous and stable even if there have ore veins below 800 m, and the ore vein occurs about 150 m below the surface so that the anomaly is not obvious. The vertical profiles showed that the width of the graphite vein is about 80 m, which is approach 77.38 m (D zone), indicating that the width of the graphite vein in the A zone was almost entirely matched with the predicted results. This proves that the width of ore-bodies can be quantitatively evaluated using the $\beta$ value.

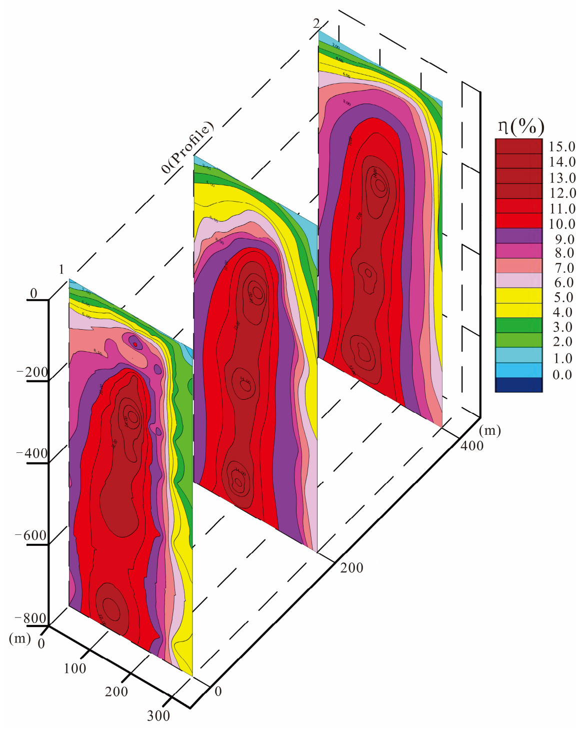


**Figure 6.** Vertical profiles of the polarizability data.

### 5.3. Anomaly Mode

The anomalies in the anomaly mode showed a linear form; most of the anomalies are distributed along with the strike of the ore-bodies, which is different from the faults represented in the metal deposits. The geological significance of the anomaly mode decomposed by S-A method, which reflects the local anomaly, need to be further studied. To figure out the significance of the high values of the abnormal mode, we selected the best anomalies area for analysis, which contained the trench and multiple drilled holes in Figure 7b. Following the strike of the ore-bodies, the grades and horizontal thicknesses of ore-bodies are shown in Table 4. Because AB was set to 1600 m in the IP method, the anomalous map of polarizability only shows a maximum depth of approximately 400 m [34,35]. According to the grade and morphology of the known ore-bodies on the profile of No. 3 in Figure 7c, we found that the high value of the anomaly pattern is related to the grade of the ore-bodies. For example, the grades and thicknesses of ore-bodies in ZK302 and QZ306 corresponded to the high values of the abnormal mode; the grade and thickness of the ore-bodies were 4.30 and 3.18 (grade), and 181.38 and 103.72 (thickness), respectively. Additionally, there are fewer graphite ores between ZK302 and QZ306, corresponding to the low-value region of the anomaly pattern. Therefore, we believe that the anomaly model can favorably reflect the degree of ore-bodies.

The comparison of the data in Table 4 with that of the anomaly mode reveals no discernible correlation between the anomalies observed in the anomaly mode and the thickness of the ore-bodies. We know that the high values of the anomaly mode corresponded with the high grade of the ore-bodies. This indicated that the values of the anomaly mode can reflect the grade degree of the ore-bodies. This conclusion is consistent with the abnormal polarizability of the wavelet transform in this region [15]. Therefore, the anomaly mode in the frequency domain can be used to judge the favorable area for mineralization in the graphite ore.

Due to the fact that the power-law exponent ($\beta$) of the background mode from the S-A model could quantitatively reflect the width of ore-bodies, we have also conducted some research on the geological significance of the power-law exponent ($\beta$) of the anomaly mode, but no significant correlation was found between the power-law exponent ($\beta$) of the anomaly mode and the feature of graphite ore. G zone is a blank area, and zone E has graphite ore, but E and G zone have the same $\beta$ value. The geological significance of the power-law exponent ($\beta$) of the anomaly mode warrants further investigation.

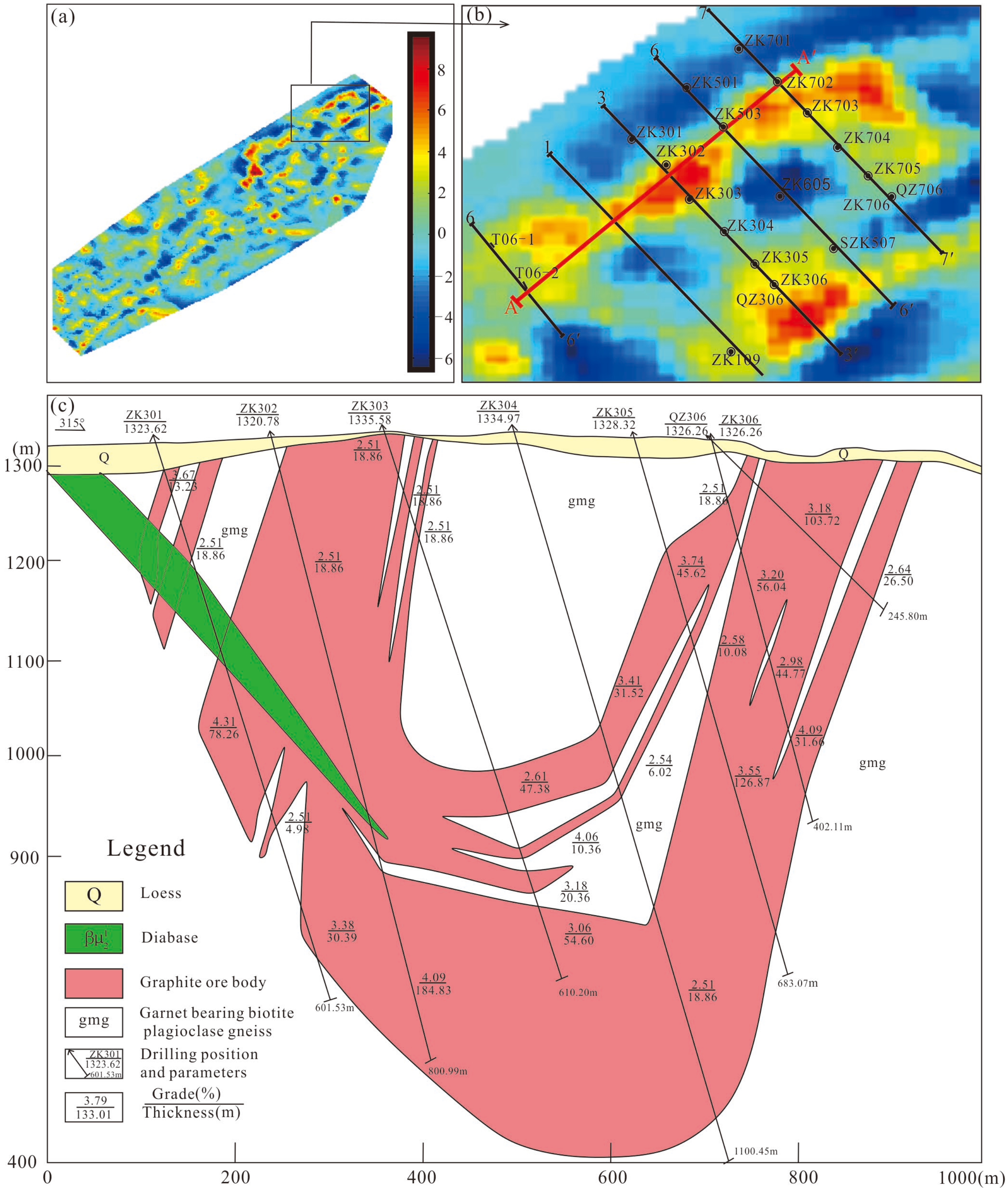

**Figure 7.** (**a**) Anomaly mode of the S-A method; (**b**) Part detail of the anomaly mode; (**c**) Detailed image of profile 3.

**Table 4.** Thickness and grade of project on the A-A′ profile.

| Profile | Project | Average Grade | Horizontal Thickness |
|---|---|---|---|
| 6 | TC6-2 | 3.23 | 5.20 |
| 3 | ZK302 | 4.30 | 122.76 |
| 5 | ZK503 | 3.61 | 129.78 |
| 7 | ZK702 | 4.24 | 29.21 |

## 6. Conclusions

This study verified that the Kriging method is the most effective interpolation method for the polarizability data, and the polarizability data have fractal characteristics. The anomaly extraction using the concentration-area (C-A) method has higher data correlation, higher accuracy, and wider range than the traditional method. The S-A method, in contrast to the C-A method, which solely enables quantitative selection of threshold values, possesses the capability to extract weak anomaly information from the coverage area.

Using the S-A method to analyze the polarizability date, we found that the background mode of the S-A model can completely depict the morphology of the graphite-bearing formation and predict the ore-bearing area. The high-value area of the background mode does not represent the width of the ore-bodies. However, the power-law exponent ($\beta$) of the background mode could be incorporated to provide a quantitative reflection of the width of the ore-bodies. We found the relationship that $\beta$ decreases as the ore-bodies width increases. The anomalies of the anomaly mode corresponded with the high grade of the ore-bodies, but the geological significance of the power-law exponent ($\beta$) has not been identified and needs further research. Combined with the study of the wavelet transform of polarizability, we believe that the anomaly mode in the frequency domain can reflect the mineralization degree of the graphite ore. In summary, the S-A method can not only classify anomalies better than the C-A method but also quantitatively predict the width and grade of ore-bodies by fractal dimension.

The background model can be used to determine the range of ore-bearing strata or the potential area, and deduce the width of the ore-bodies based on the $\beta$ value. Using the abnormal model to judge the grade of the graphite ore. By integrating the background and anomaly modes of the S-A method, we can quantitatively predict and effectively select a high-grade target for future exploration. This conclusion can be extended to other graphite deposits or sedimentary-metamorphic deposits containing conductive minerals.

**Author Contributions:** Conceptualization, Y.L. and Q.X.; methodology, Y.L.; software, Y.L.; validation, Y.L.; formal analysis, Y.L.; investigation, E.P.; resources, K.J.; data curation, Y.L.; writing—original draft preparation, Y.L.; writing—review and editing, Y.L.; visualization, K.J.; supervision, Q.X.; project administration, Q.X.; funding acquisition, E.P. All authors have read and agreed to the published version of the manuscript.

**Funding:** This research was funded by Shanxi Geological Group in China, grant number 2022-14; Shanxi government in China, grant number ZJZC-231FW125-16.

**Data Availability Statement:** The data presented in this study are available on request from the corresponding author.

**Conflicts of Interest:** Authors Kenan Jiang and Kenan Jiang was employed by the company 217 Team of Shanxi Geological Group. The remaining authors declare that the research was conducted in the absence of any commercial or financial relationships that could be construed as a potential conflict of interest.

## References

1. Mandelbrot, B.B.; Freeman, W.H. The fractal geometry of nature. *Earth. Surf. Proc. Land.* **1982**, *8*, 406. [CrossRef]
2. Agterberg, F.P. Geomathematics: Theoretical foundations, applications and future developments. *Quant. Geol. Geostat.* **2014**, *18*, 369–411. [CrossRef]

3. Zhao, M.Y.; Xia, Q.L.; Wu, L.R.; Liang, Y.Q. Identification of Multi-Element Geochemical Anomalies for Cu-Polymetallic Deposits Through Staged Factor Analysis, Improved Fractal Density and Expected Value Function. *Nat. Resour. Res.* **2022**, *31*, 1867–1887. [CrossRef]
4. Zuo, R.; Cheng, Q.; Agterberg, F.; Xia, Q. Application of singularity mapping technique to identify local anomalies using stream sediment geochemical data, a case study from Gangdese, Tibet, western China. *J. Geochem. Explor.* **2009**, *101*, 225–235. [CrossRef]
5. Cheng, Q.M.; Agterberg, F.P.; Ballantyne, B.S. The separation of geochemical anomalies from background by fractal method. *J. Geochem. Explor.* **1994**, *43*, 91–95. [CrossRef]
6. Cheng, Q.M.; Xu, Y.; Grunsky, E. Integrated spatial and spectrum method for geochemical anomaly separation. *Nat. Resour. Res.* **2000**, *9*, 43–52. [CrossRef]
7. Cheng, Q.M. Multiplicative cascade processes and information integration for predictive mapping. *Nonlinear Process. Geophys.* **2012**, *19*, 57–68. [CrossRef]
8. Liang, Y.Q.; Zhang, S.T.; Wang, G.W. Alteration from ETM+ data rating based on fractal technologies. *Adv. Mater. Res.* **2012**, *457*, 1202–1206. [CrossRef]
9. Wang, W.L.; Zhao, J.; Cheng, Q.M. Analysis and integration of geo-information to identify granitic intrusions as exploration targets in southeastern Yunnan District, China. *Comput. Geosci.* **2011**, *37*, 1946–1957. [CrossRef]
10. Zuo, R.G.; Wang, J.L. Arcfractal: An arcgis add-in for processing geoscience date using fractal/multifractal models. *Nat. Resour. Res.* **2019**, *29*, 3–12. [CrossRef]
11. Jiang, C.; Li, S.H.; Fu, S.; Xie, Z.L.; Liao, H.W. Tectonic fractal and metallogenic prediction in Northwest Dayao mountain, Guangxi. *Acta Geosci. Sin.* **2021**, *42*, 514–526.
12. Daneshvar, S.L.; Rasa, I.; Rashidnejad, O.N.; Moarefvand, P.; Afzal, P. Application of concentration-volume fractal method in induced polarization and resistivity data interpretation for Cu-Mo porphyry deposits exploration, case study: Nowchun Cu-Mo deposit, SE Iran. *Nonlinear Process. Geophys.* **2012**, *19*, 431–438. [CrossRef]
13. Rakoto, H.A.; Riva, R.; Ralay, R.; Boni, R. Evaluation of flake graphite ore using self-potential (SP), electrical resistivity tomography (ERT) and induced polarization (IP) methods in east coast of Madagascar. *J. Appl. Geophys.* **2019**, *169*, 134–141. [CrossRef]
14. Zhang, Y.; Zhou, Y.-Z.; Wang, L.-F.; Wang, Z.-H.; He, J.-G.; An, Y.-F.; Li, H.-Z.; Zeng, C.-Y.; Liang, J.; Lü, W.-C.; et al. The recognition and extraction of geochemical composite anomalies: A case study of Pangxidong area. *Acta Geosci. Sin.* **2011**, *32*, 533–540. [CrossRef]
15. Liang, Y.Q.; Xia, Q.L.; Zhao, M.Y.; Bi, R.; Liu, J.K. Application and Significance of the Wavelet–Fractal Method on the Data of the Induced Polarization Method in the Graphite Deposits of Datong, China. *Minerals* **2023**, *13*, 760. [CrossRef]
16. Srivastava, G.S.; Merriam, D.F. Use of the power spectrum in characterizing structural surfaces. *Comput. Geosci.* **1980**, *6*, 87–94. [CrossRef]
17. Cressie, N.A.C. *Statistics for Spatial Data, Revised Edition*; Wiley: Hoboken, NJ, USA, 2015; ISBN 9780471002550.
18. Wang, W.L.; Cheng, Q.M.; Tang, J.X.; Pubuciren; Song, Y.; Li, Y.B.; Liu, Z.B. Fractal/multifractal analysis in support of mineral exploration in the Duolong mineral district, Tibet, China. *Geochem. Explor. Environ. Anal.* **2017**, *17*, 261–276. [CrossRef]
19. Cheng, Q.M. Non-Linear theory and Power-Law models for information integration and mineral resources quantitative assessments. *Math. Geosci.* **2008**, *40*, 503–532. [CrossRef]
20. Liang, Y.Q.; Zhao, Y.; Wu, G.C.; Zhang, Y.; Xia, Q.L. Research on geochemistry characteristics and genesis of the graphite deposit in Xinrong district of Datong city, Shanxi province. *Acta Geosci. Sin.* **2020**, *41*, 827–834. [CrossRef]
21. Berry, M.V.; Lewis, Z.V. On the Weierstrass-Mandelbrot fractal function. *Proc. R. Soc. A Math. Phys. Eng. Sci.* **1980**, *370*, 459–484. [CrossRef]
22. Xia, Q.L.; Zhang, S.T.; Zhao, P.D.; Jin, Y.Y. Power-law and mineral prediction. *J. Chengdu Univ. Technol.* **2003**, *30*, 453–456. (In Chinese with English abstract)
23. Cheng, Q.M. Mapping singularities with stream sediment geochemical data for prediction of undiscovered mineral deposits in Gejiu, Yunnan province, China. *Ore Geol. Rev.* **2007**, *32*, 314–324. [CrossRef]
24. Carlson, A. Spatial distribution of ore deposits. *Geology* **1991**, *19*, 111–114. [CrossRef]
25. Thomas, H.W. Some Distinctions between self-similar and self-affine estimates of fractal dimension with case history. *Math. Geol.* **2000**, *32*, 319–335. [CrossRef]
26. Agterberg, F.P. Fractals and spatial statiscs of point patterns. *J. Earth Sci.* **2013**, *24*, 1–11. [CrossRef]
27. Cheng, Q.M. A new model for quantifying anisotropic scale invariance and for decomposition of mixing patterns. *Mathmatical Geol.* **2004**, *36*, 345–460. [CrossRef]
28. James, R.C.; Wiliam, B.B. On the practice of estimating fractal dimension. *Math. Geol.* **1991**, *23*, 945–958. [CrossRef]
29. Cheng, Q.M. Spatial and scaling modelling for geochemical anomaly separation. *J. Geochem. Explor.* **1999**, *63*, 175–194. [CrossRef]
30. Huang, J.N.; Zhao, B.B.; Chen, Y.Q.; Zhao, P.D. Bidimensional empirical mode decomposition (BEMD) for extraction of gravity anomalies associated with gold mineralization in the Tongshi gold field, Western Shandong Uplifted Block, Eastern China. *Comput. Geosci.* **2010**, *36*, 987–995. [CrossRef]
31. Cheng, Q.M. Quantitative simulation and prediction of extreme geological events. *Sci. China-Earth Sci.* **2022**, *6*, 65–83. [CrossRef]
32. Liang, Y.Q.; Xia, Q.L.; Zhang, Y.; Zhao, Y. Geochemical characteristics and indication of graphite deposits in Xinrong Region, Shanxi, China. *Geochem. Explor. Environ. Anal.* **2022**, *22*, 52–64. [CrossRef]

33. Liang, Y.Q.; Zhang, Y.; Li, Y.; Liu, J.K. *Detailed Investigation Report of Graphite Mine in Qilicun-Duijiugou of Xinrong District, Datong, Shanxi*; Government of Shanxi Province: Taiyuan, China, 2021. (In Chinese with English abstract)
34. Liang, Y.Q. *Metallogenic Model and Prediction of Graphite Ore in Xinrong District of Datong, Shanxi Province, China*; China University of Geosciences: Wuhan, China, 2023. (In Chinese with English abstract)
35. Zhang, Y.; Liang, Y.Q.; Li, Y.; Wu, G.C. *General Survey Report of Graphite Mine in Liumudi of Xinrong District, Datong, Shanxi*; Government of Shanxi Province: Taiyuan, China, 2019. (In Chinese with English abstract)
36. Pelton, W.H.; Ward, S.H.; Hallof, P.G.; Sill, W.R.; Nelson, P.H. Mineral discrimination and removal of inductive coupling with multifrequency IP. *Geophysics* **1978**, *43*, 588–609. [CrossRef]
37. Seigel, H.; Nabighian, M.; Parasnis, D.S.; Vozoff, K. The early history of the induced polarization method. *Lead. Edge* **2007**, *3*, 312–321. [CrossRef]
38. Gianluca, F.; James, R.; Andrew, B.; Andrew, B.; Aurelie, G.; Anders, V.C.; Esben, A. Resolving spectral information from time domain induced polarization data through 2-D inversion. *Geophys. J. Int.* **2013**, *2*, 631–646. [CrossRef]
39. Well, A.; Slater, L.; Nordsiek, S. On the relationship between induced polarization and surface conductivity: Implications for petrophysical interpretation of electrical measurements. *Geophys. J. Soc. Explor. Geophys.* **2013**, *78*, 315–325. [CrossRef]
40. Ghorbani, A.; Camerlynck, C.; Florsch, N.; Cosenza, P.; Revil, A. Bayesian inference of the Cole-Cole parameters from time and frequency-domain induced polarization. *Geophys. Prospect.* **2007**, *55*, 589–605. [CrossRef]
41. Seigel, H. Mathematical formulation and type curves for induced polarization. *Geophysics.* **1959**, *24*, 547–565. [CrossRef]
42. Marshall, D.J.; Madden, T.R. Induced polarization: A study of its causes. *Geophysics.* **1959**, *24*, 790–816. [CrossRef]
43. Gurin, G.; Titov, K.; Ilyin, Y.; Tarasov, A. Induced polarization of disseminated electronically conductive minerals: A semi-empirical model. *Geophys. J. Int.* **2015**, *200*, 1555–1565. [CrossRef]
44. Bhattacharya, B.B.; Biswas, D.; Kar, G.; Ghosh, H. Geoelectric exploration for graphite in the Balangir district, Orissa, India. *Geoexploration* **1984**, *22*, 129–143. [CrossRef]
45. Okay, G.; Cosenza, P.; Ghorbani, A.; Camerlynck, C.; Cabrera, N.F.; Revil, A. Localization and characterization of cracks in clay-rocks using frequency and time-domain induced polarization. *Geophys. Prospect.* **2013**, *61*, 134–152. [CrossRef]
46. Tarasov, A.; Titov, K. Relaxation time distribution from time domain induced polarization measurements. *Geophys. J. Int.* **2007**, *170*, 31–43. [CrossRef]
47. Oldenburg, D.W.; Li, Y.G. Inversion of induced polarization data. *Geophysics* **1994**, *59*, 1327–1341. [CrossRef]